# Uncertainty assessment of a green-wavelength LiDAR in laboratory environments

Yu Lan [1 (0009-0000-4023-5857)], Ji Yang[1(0009-0001-8091-2434)], Mario Kolling[1(0009-0003-7357-235X)], Alexander Dorndorf[1 (0000-0002-4396-2694)] & Jens-André Paffenholz [1 (0000-0003-1222-5568)]

[1] Institute of Geotechnology and Mineral Resources – Geomatics, Clausthal University of Technology, yu.lan@tu-clausthal.de

## 1 Motivation and challenge

A novel green-band Light Detection and Ranging (LiDAR) system specifically for underwater metrology, termed Underwater LiDAR (ULi) system, has recently been developed by the Fraunhofer Institute for Physical Measurement Techniques (IPM). The system is based on Time-Of-Flight (TOF) ranging and is capable of achieving millimeter-level ranging performance underwater. Multiple studies have already demonstrated that this LiDAR exhibits reliable performance in underwater scenarios (see Section 2). In the present use case, the sensor is operated at the waterline, so that its performance in the medium air is of particular interest. Additionally, the ULi system is applied for waterline data acquisition in underground adits with an approximate height of 2.25 m. Given a typical water surface-to-crown clearance of about 1.75 m and an in the medium air LiDAR field of view (FOV) of ~60°, this study evaluates the ULi system performance over distances from 2 to 5 m in the medium air to support reliable mapping of the adits environment.

The main challenge associated with this system is that its performance characteristics in air are up to now not deeply investigated, despite the fact that its underwater performance has been validated in several studies (see Section 2). Because the LiDAR is customized explicitly for underwater operation, its optical design and system parameters may not directly transfer to measurements that involve a significant path in air. For the targeted waterline application, it is therefore necessary to thoroughly characterize and quantify the in-air performance of the sensor. Only by doing so it can be ensured that millimeter-level ranging performance is maintained when the LiDAR is used in configurations that deviate from its original underwater design conditions. Based on this, the measurements of ULi system in the medium air is evaluated using the terrestrial laser scanner (TLS) Zoller+Fröhlich (Z+F) IMAGER 5016A (IMAGER) (Zoller+Fröhlich 2026) as a reference. For the ULi, the point cloud density distribution, precision, and bias are analyzed in this work.

In this paper, Section 2 reviews related work on the ULi system. Section 3 describes the methods used to assess the ULi system, focusing on precision and systematic bias. Section 4 presents the experimental design and the results. Finally, Section 5 summarizes the results and describe the future work.

## 2    Literature review

The Fraunhofer IPM developed a submersible ULi system in a pressure-resistant housing for deployment on stationary or mobile platforms to support underwater topography and infrastructure inspection. Initial tests in controlled water environments produced point clouds with promising resolution, accuracy and acquisition speed, indicating good potential for precise subsea mapping and inspection applications (Werner et al. 2023; Fraunhofer IPM, 2025). According to Walter et al. (2025), the ULi system was systematically tested in two laboratory scenarios and one real-world scenario to assess its suitability for high-resolution monitoring of underwater infrastructure. In a close-range static tank experiment under clear water conditions (NTU = 0), the ULi system was able to detect man-made and organic structures down to 2.36 mm at a close range (≤ 0.56 m), demonstrating millimeter-scale level of detail. A second static laboratory experiment from 1.03 m to 8.03 m, using a Boehler star target, showed that arc segments of 2.95 mm could be fully resolved at distances up to 8.03 m. In contrast, the field trial in the river Elbe yielded no meaningful reflections from infrastructure targets, leading the authors to conclude that the ULi system was not suitable for operation in water bodies with turbidity ≥ 6 NTU (or Secchi depth ≤ 1.10 m). Heffner et al. (2025) applied static scans of a Boehler star, spheres and metal plates at different ranges and for varying turbidity levels. Repeated measurements on a metal plate were used to derive precision and accuracy metrics. Additionally, they reported a range precision of 1.95 mm and a mean relative range accuracy of 6.01 mm. Further they demonstrated that small objects such as shells and water plants can still be clearly identified in low-turbidity conditions.

## 3    Methodology

### 3.1    Plane-based precision

Spatial variations in point density are common in LiDAR-based point clouds. Importantly, density anomalies may indicate issues in the point cloud and can lead to errors in derived products (Petras et al. 2023). Accordingly, analyzing the spatial distribution of the point density in point clouds is crucial. First, the center of the 4-fold and BOTA-8 targets are estimated according to the method of Janßen et al. (2019). Subsequently, the Helmert 3D transformation is applied to estimate a rigid transformation ($R$, $t$) between IMAGER and ULi system and the scale is set to be 1 (Paffenholz & Bae 2012).

$$x_{ULi,k} = Rx_{IMAGER,k} + t \tag{1}$$

Let $k = 1$ to $K$, where $K$ indexes the corresponding target centers. Here, $R$ is the rotation matrix and $t$ is the translation vector between the frame of IMAGER and the ULi system. $x_{IMAGER,k}$ is the coordinate from IMAGER. Using the registration targets, the alignment quality is assessed from the residuals at these control points after applying the estimated rigid transformation. The overall registration error $e_{reg}$ is quantified as the mean 3D misclosure magnitude after transformation. Here, the point density of the IMAGER and ULi system is compared after alignment, with a voxel size of 0.1 m × 0.1 m × 0.1 m for sampling. The

resulting voxel occupancies enable a direct comparison of how uniformly the ULi system samples the scene relative to the IMAGER reference.

For the precision evaluation, the focus is on the random component of the 3D point cloud uncertainty and quantify it from orthogonal point-to-plane residuals. The plane parameters are estimated within a Gauss-Helmert adjustment, where observation corrections are applied to the measured 3D points to satisfy the planar condition. In the absence of point-wise covariance information, all observations are assumed uncorrelated and of identical precision, which reduces the adjustment to a standard orthogonal-distance plane fit solved by a singular value decomposition (SVD) based formulation. The analysis is conducted at the point level using a planar target as a controlled reference geometry (Schaffrin et al. 2006; Neitzel, 2010). Additionally, to mitigate the influence of potential board warping, the target surface is partitioned into 100 small patches (0.1 m × 0.1 m) and exclude patches affected by occlusions (e.g., screws). The size should keep the local surface approximately planer and ensure enough points per patch for stable precision statistics. The plane is fitted for each patch and expressed as:

$$\boldsymbol{n}^T \boldsymbol{x}_{ULi} + d = 0, \|\boldsymbol{n}\| = 1 \tag{2}$$

Where $\boldsymbol{n}$ denotes the unit normal vector of the plane. Let $\boldsymbol{x}_{ULi}$ denotes the coordinate in the ULi frame and $\boldsymbol{d}$ is the plane offset. To avoid inflating the precision estimated by boundary-related effects, points potentially affected by edge effects are excluded by intensity-based filtering. Random point dispersion is then quantified from the distribution of orthogonal residuals to the fitted plane (see Eq.3). The spread of these normal-direction residuals provides a direct estimation of the point-level precision under the given measurement conditions. Where $i$ is the number of repeated scans and $p$ is the point index in the patch. For each point $\boldsymbol{x}_{ULi,i,j,p}$ in the selected patch $j$, the signed orthogonal residual is:

$$r_{i,j,p} = \hat{\boldsymbol{n}}^T \boldsymbol{x}_{ULi,i,j,p} + \hat{d} \tag{3}$$

The plane-fit residual dispersion is summarized as (Dewez et al. 2016):

$$\hat{\sigma}_{i,j} = \sqrt{\frac{1}{N_{i,j}} \sum_{p=1}^{N_{i,j}} r_{i,j,p}^2} \tag{4}$$

Where $N_{i,j}$ is the number of points in the patch $j$ for repetition $i$ and it is used to compute the plane residual $\hat{\sigma}_{i,j}$. Multiple repetitions at each scanning distance enable the assessment of range-dependent repeatability, reported as the distribution of the residual-dispersion metric across repeats.

## 3.2    Bias analysis

The systematic bias of the green-wavelength ULi system is assessed via the IMAGER by selecting a hybrid board that combines a ChArUco pattern with dedicated geometric targets (e.g., 4-fold target) (see Fig. 1). The rigid body transformation is estimated by using the well distributed targets (see Section 3.1). Subsequently, the alignment of the IMAGER and ULi system point cloud is given. The bias estimation is performed using the Multiscale Model-to-

Model Cloud Comparison (M3C2) distance using CloudCompare v2.14.beta (Dec. 28 2025) (Lague et al. 2013). The IMAGER point cloud within the selected patch on the hybrid board are used as core points to ensure a stable reference sampling. To mitigate edge effects or mixed-pixel effects caused by dense black and white transitions target borders and hole rims, the patches which located away from these regions are manually extracted from the hybrid board (see Fig. 7). The local surface normals are estimated at the selected core points, and the M3C2 distances are then computed as the separation between the two point clouds along these normals using a projection cylinder and robust statistics.

# 4     Experiments

## 4.1     Precision of the 3D point cloud of the ULi system

### 4.1.1  3D point cloud density evaluation of the ULi system

The ULi system is different from traditional TLS. According to the pulse settings, it produces 100,000 pts/s (skipped pulses = 0). To accommodate 3D LiDAR scanning on a mobile platform, the motor speed is set to 25 Hz and the scan pattern is circular (spiral-shaped circle) so each revolution generates 4,000 pts/s (Fraunhofer IPM, 2025). The density of the point cloud will differ from that of a traditional TLS, from which the point cloud exhibits a regular, raster-like distribution, but the point cloud density of the ULi system varies with the scanning radius. In theory, the radius change speed can be increased arbitrarily, however, to balance the inter-ring spacing to the millimeter range and to avoid overheating the ULi system during airborne operation, the radius change speed is set to 0.002 Hz. The laser class in the medium air is set to be 2M which is the lowest power of the ULi system. The configuration of the ULi system is shown in Table 1.

**Table 1:** Configuration of the ULi system in airborne operation.

| Configuration | Value |
|---|---|
| Motor speed (Hz) | 25 |
| Filter type (Laser class) | Adjustment (2M) |
| Scan pattern | Circle |
| Radius change speed (Hz) | 0.002 |
| Medium refractive index | 1.0003 |
| Skip pulse | 0 |

The setup of the IMAGER and ULi system is shown in Fig. 1. Out of the in the experimental scene available targets, 7 well-distributed targets are chosen for the mutual point cloud registration. The ULi system is positioned nearly perpendicular to the object board, so the incidence angle is 90±2 degree with respect to the board plane.
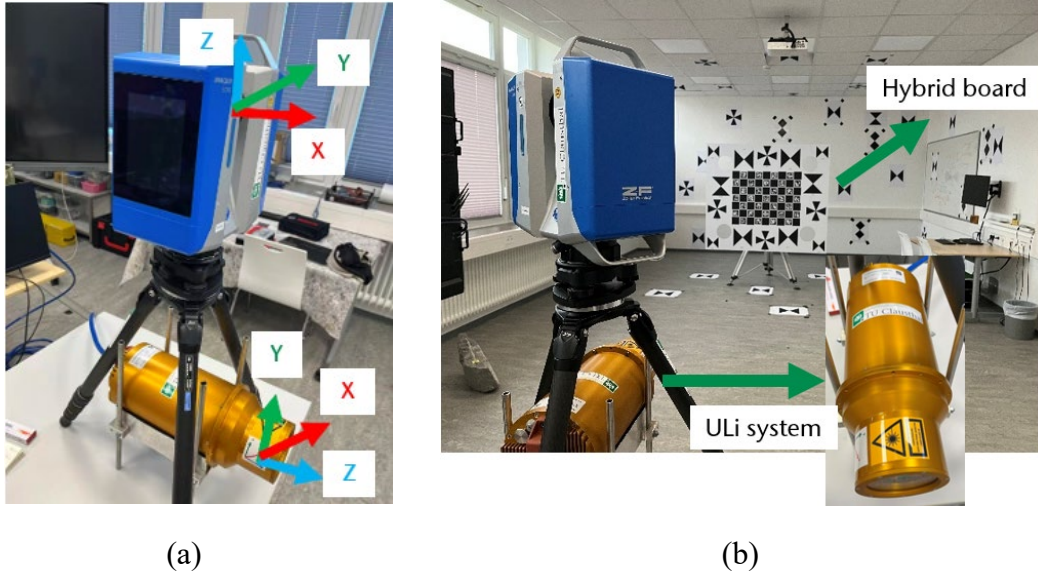
(a)                                                                    (b)

**Fig. 1:** (a) Setup of the IMAGER and ULi system; (b) Setup of the targets for mutual point cloud registration.

To provide a qualitative overview of the acquired data, Fig. 2 shows an intensity-colored point cloud of the experimental scene. ULi's spiral center is the ULi scan starts at the location corresponding to the minimum scan radius.
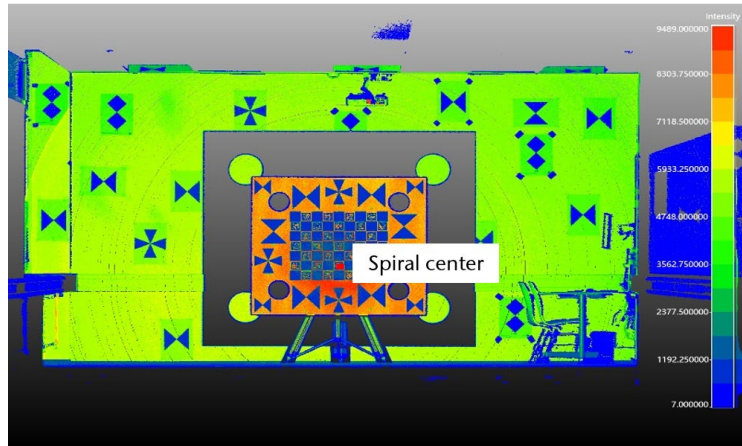


**Fig. 2:** Intensity-colored point cloud acquired by the ULi system, illustrating the spiral scanning pattern on the planar target and surrounding scene.

In comparison, the IMAGER used the ultra-high-resolution setup, in which the point spacing is 1.6 mm @10 m. In this setup, the two point clouds are mutually registered using 7 corresponding targets. The overall registration error is $e_{reg} = 1.7$ mm. According to Section 3.1, the IMAGER point cloud is transformed into the ULi system coordinate frame. The result of the spacing comparison is shown in Fig. 3.
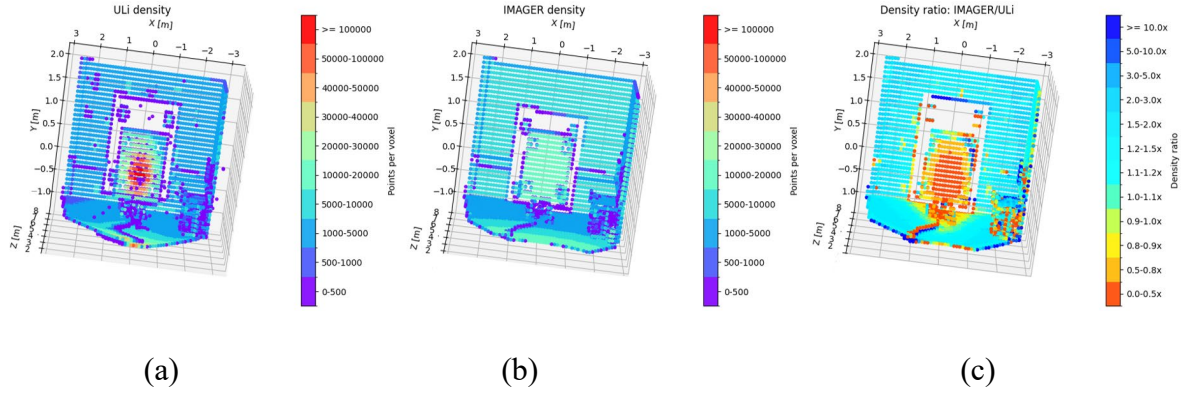
<center>(a)                                    (b)                                    (c)</center>

**Fig. 3:** Point cloud density of (a) the ULi system and (b) the IMAGER as well as (c) the density ratio map of IMAGER and ULi system.

Fig. 3 compares the voxel-based sampling density for the ULi system and the IMAGER in a common reference frame, reported as the number of points per voxel (Fig. 3(a) and (b)). The ULi system shows a pronounced acquisition imprint with spatially non-uniform point counts and characteristic spiral patterns, consistent with its rotating scan trajectory and the resulting range-dependent spatial sampling. The IMAGER exhibits a more homogeneous, raster-like distribution over the same volume. The voxel-wise density ratio map in Fig. 3(c), defined as (density of IMAGER)/(density of ULi system), makes this contrast explicit: ratio $\approx 1$ indicates comparable sampling, ratio $< 1$ (ULi is denser) and ratio $> 1$ (IMAGER is denser) occur in different regions, demonstrating that the density advantage is strongly location-dependent. It can be clearly observed on the hybrid board @5 m that the ULi point density is highest near the spiral center (see Fig. 2). As the scan radius increases, the points become sparser, and the ULi density drops below that of the IMAGER. This motivates restricting subsequent cross-sensor comparisons to the common overlap and explicitly accounting for density-related effects.

### 4.1.2  Precision analysis of the point cloud of the ULi system

A 1 m × 1 m white board made of Resopal panel (Walter et al. 2025) is used to evaluate the precision (repeatability) of the ULi system (Fig. 4). The spiral scan center is aligned with the geometric center of the board.
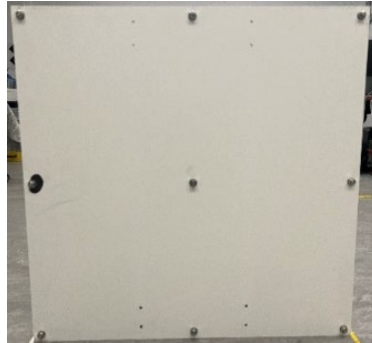


**Fig. 4:** The measurement board used for the repetition evaluation.

The spatial variability of point-level precision on the planar reference board is visualized using a patch-wise analysis and is shown in Fig. 5. The board surface is subdivided into a regular grid of squared patches, and patches affected by occlusions (e.g., screws), boundary effects are excluded (blank cells). The values reported in the heatmaps in Fig. 5 are the mean values $\hat{\mu}_{\hat{\sigma}_j}$ of $\hat{\sigma}_j$ for each patch computed from measurements acquired at distances of (a) 2 m, (b) 3 m, (c) 4 m and (d) 5 m, using an identical color scale to enable direct comparison. In addition, each patch is assigned a corresponding index above the $\hat{\mu}_{\hat{\sigma}_j}$.
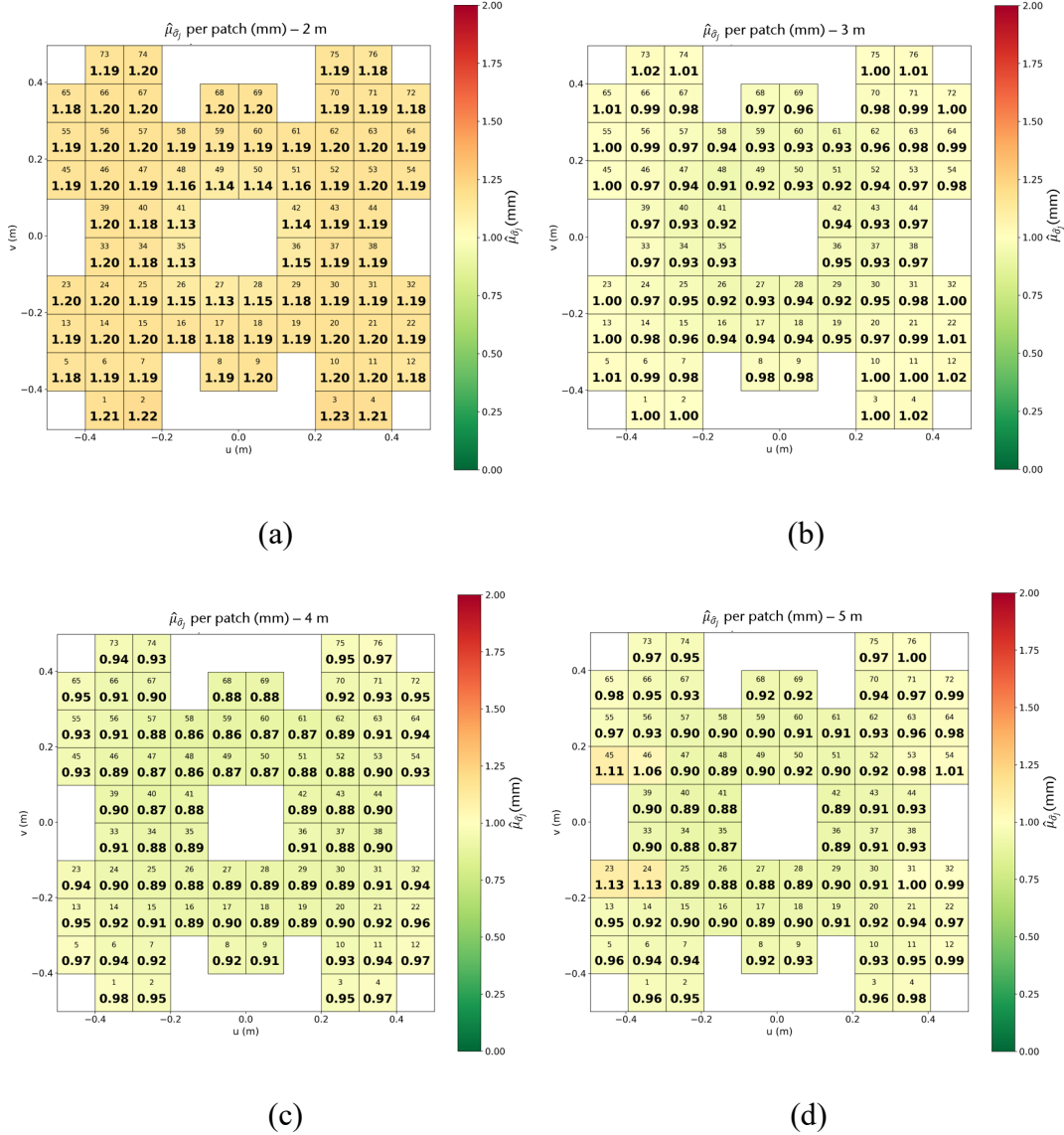


(a)



(b)



(c)



(d)

**Fig. 5:** Mean values $\hat{\mu}_{\hat{\sigma}_j}$ per patch averaged over 10 repeated scans in the board local coordinate system for distances ranging from (a) 2 m to (d) 5 m.

Overall, Fig. 5 shows that within each distance, slightly larger $\hat{\mu}_{\hat{\sigma}_j}$ values tend to occur near the outer regions or in areas with reduced data support, which might be consistent with residual edge effects, local incidence-angle differences or lower sampling density.

Comparing distances, the absolute $\hat{\mu}_{\hat{\sigma}_j}$ level decreases from 2 m to 4 m: at 2 m most patches are around ~1.13 to 1.23 mm, whereas at 3 m they are typically ~0.91 to 1.02 mm, and at 4 m mainly ~0.86 to 0.98 mm. At 5 m, $\hat{\mu}_{\hat{\sigma}_j}$ remains in a similar range for most patches (~0.87 to1.13 mm). Overall, the patch-wise $\hat{\mu}_{\hat{\sigma}_j}$ remains on the order of ~1 mm from 2 m to 5 m. In principle, one would expect the precision to degrade with increasing distance due to growing ranging uncertainty. However, the observed $\hat{\mu}_{\hat{\sigma}_j}$ values show the opposite trend, which suggests that the patch-wise residual dispersion is not influenced by intrinsic range noise alone but is strongly influenced by the sampling geometry. In these measurements, the ULi point density is strongly non-uniform across the board (higher near the spiral center and lower toward larger scan radius). With increasing distance (3 to 5 m), the effective board coverage contracts toward the spiral center, thereby changing the local point cloud density and biasing the analysis toward a smaller, centrally sampled subset. Consequently, the observed trend should be interpreted in the context of distance-dependent coverage and point cloud density, rather than taken as direct evidence of improved sensor precision.

In Fig. 6, the repeatability of the patch-wise precision estimate is assessed across repeated scans. For each distance from 2 to 5 m, the heatmap reports the standard deviation of $\sigma_{rep}$ across repetitions for each patch. Lower values indicate that the estimated precision is stable across repeats, whereas higher values reveal patches where the precision estimate is more variable.
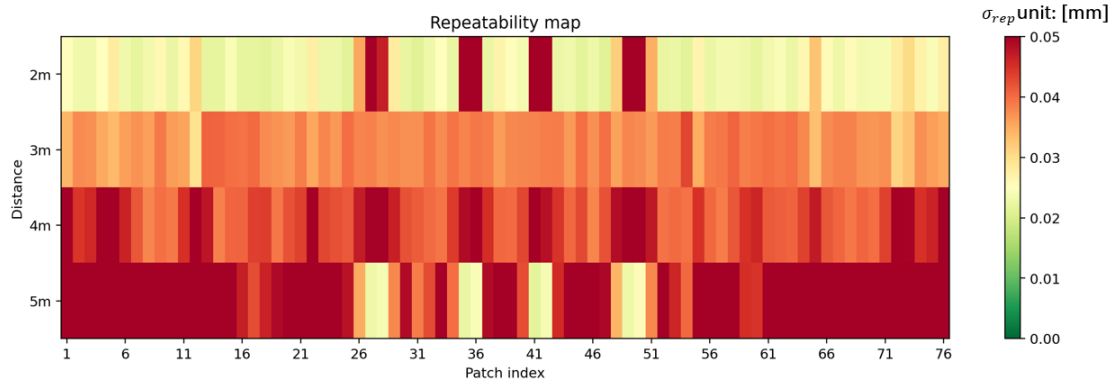


**Fig. 6:** Heat map of the ULi system repeatability.

Overall, Fig. 6 indicates that the repeatability of the precision estimate is high, as most patches show $\sigma_{rep}$ values in the order of only a few hundredths of a millimeter (~0.01 to 0.05 mm). This suggests that the patch-wise $\hat{\mu}_{\hat{\sigma}_j}$ values reported are not driven by random fluctuations between scans but are largely reproducible under identical acquisition conditions.

A clear range-dependent pattern is visible: at 2 m, most patches exhibit low variability (predominantly green to yellow), with only a few isolated patches showing elevated $\sigma_{rep,j}$. At 3 m and 4 m, the variability generally increases, indicating that the precision estimate becomes more sensitive to local sampling conditions as distance grows. At 5 m, many patches reach the upper end of the displayed scale, implying that repeatability is most challenging at the 5 m distance. This behavior is consistent with the reduced sampling density and signal strength at larger distances, where small changes in point density and distribution and local incidence angle

distribution can cause stronger fluctuations in the estimated $\hat{\mu}_{\hat{\sigma}_j}$ from scan to scan. Additionally, a spatial pattern is observed: at 2 m, patches closer to the spiral center exhibit relatively higher $\sigma_{rep,j}$ values, whereas with increasing distance this centrally elevated trend becomes less pronounced. This likely reflects the high sampling density and small footprint at short distances, which make the patch-wise residual metric more sensitive to subtle scan-to-scan changes in local sampling geometry. However, further experiments are needed to verify which factor(s) primarily drive this effect.

## 4.2 Preliminary sensor bias estimation

Bias evaluation is carried out on the hybrid board by defining 5 planar analysis patches (Patch 1 to Patch 5, each with a size of $0.1 \times 0.1$ m) on the board surface @5 m and acquiring nine ULi system point clouds under identical static conditions (Fig. 7). A single IMAGER point cloud serves as the core points (Fig. 1). The IMAGER point cloud is aligned with the ULi system frame using the previously determined rigid alignment from the targets in the laboratory. Then all bias-related quantities are computed patch-wise and summarized across the nine point clouds to obtain a repeat-averaged systematic offset and its repeatability for each patch.
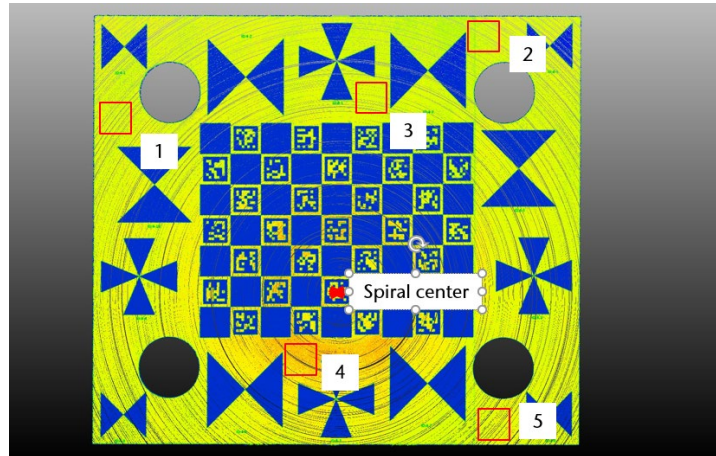


**Fig. 7:** Sampling patch in the hybrid board.

The used configuration for the M3C2 calculation using CloudCompare is shown in Table 2.

**Table 2:** Configuration of M3C2 calculation.

| Configuration (mm) | Value |
| --- | --- |
| Normal scale | 30 |
| Search scale | 10 |
| Subsample radius | 3.2 |
| Search depth | 30 |
| Registration error | 1.7 |

In Fig. 8, the patch-wise M3C2 bias between the aligned point clouds is summarized for five representative planar patches extracted from the common overlap. For each patch, the distribution of M3C2 distances is reduced to two location measures, the mean (red) and median (green).
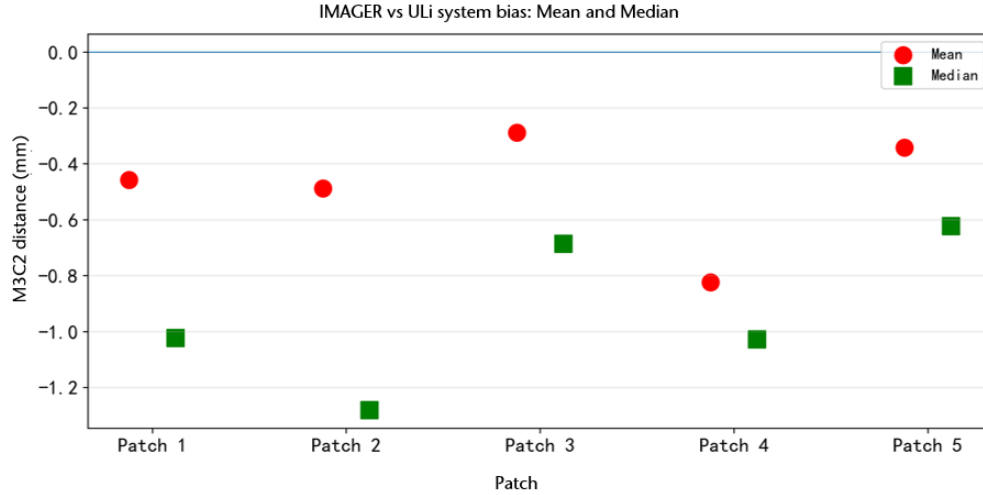


**Fig. 8:** Mean and median of M3C2 distances per patch.

Across all five patches, both the mean and the median M3C2 distances are consistently negative, indicating it might have a systematic offset between ULi system and IMAGER. With the IMAGER selected as the core point, the reported distances represent signed separations measured along the IMAGER-derived normals toward the compared ULi cloud. Under this condition, the predominantly negative values imply that the ULi system surface is, on average, shifted in the negative normal direction relative to the IMAGER surface. The patch-wise means are on the order of approximately $-0.3$ to $-0.8$ mm, while the medians span roughly $-0.6$ to $-1.3$ mm. Medians are systematically more negative than means, suggesting an asymmetric distance distribution and supporting the median as the robust estimator of the central tendency for bias reporting. Patch-to-patch differences are visible, with Patch 2 exhibiting the strongest negative median and Patch 3 showing the smallest magnitude of negative bias.

These patch-level bias estimates should be interpreted in conjunction with the estimated registration error, as a systematic M3C2 offset can arise from a combination of sensor-related bias and alignment effects. The IMAGER-to-ULi M3C2 distance from different epochs is analyzed. Fig. 9 reveals a clear time-dependent drift (with the IMAGER as the core point and the first ULi system epoch defined the temporal baseline, i.e., time are reported relative to the first epoch) across epochs that is coherent over all patches.
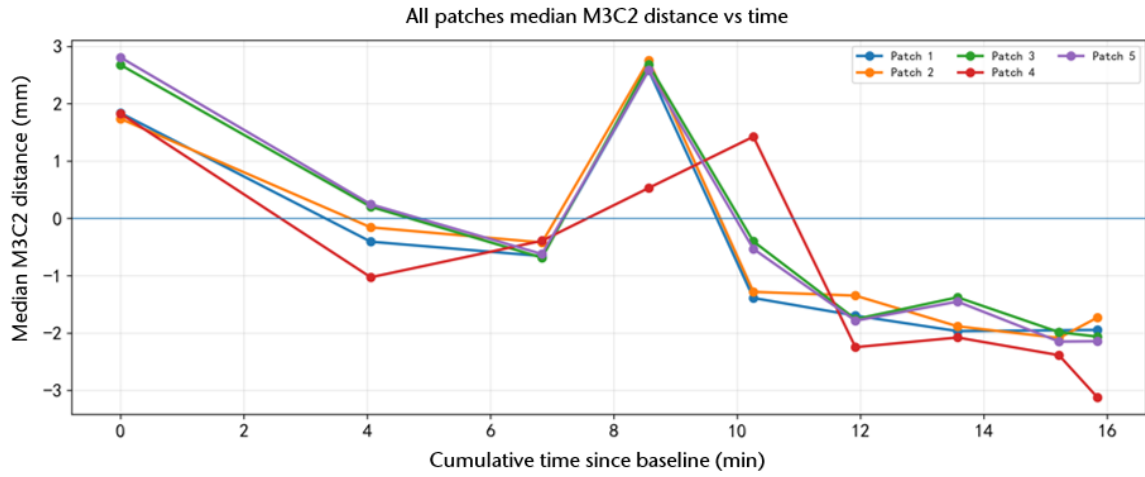
**Fig. 9:** Median M3C2 distances per patch over time.

As shown in Fig. 9, the patch-wise M3C2 distances between the IMAGER reference and the corresponding ULi system epochs are summarized as epoch-level medians and plotted against the cumulative time since the first epoch of the ULi system. Over the ∼16 min measurement sequence, the offsets exhibit a largely coherent temporal evolution across all patches: values shift from initially positive or near-zero levels to predominantly negative levels at later times, reaching approximately −1 to −3 mm towards the end of the sequence. The strong inter-patch coherence indicates that the dominant contribution is a global and time-dependent component affecting the ULi to IMAGER relative geometry. Superimposed on this overall trend, a short-lived positive peak is visible around ∼8 to 9 min (epoch four) and patch-specific deviations from the overall trend occur (e.g., Patch 4 around ∼10 min to 11 min), which may reflect incidence-angle and sampling-density differences. In Fig. 9, the result is comparable to the single-epoch precision scale ($\hat{\mu}_{\hat{\sigma}_j} \approx 1$ mm from Section 4.1.2) and remains within roughly ∼$3\hat{\mu}_{\hat{\sigma}_j}$ (≈3 mm).

A potential contributing factor is the ULi system's spiral acquisition geometry: because the spiral radius is intentionally set to change slowly (radius-change speed 0.002 Hz) to maintain a comparable point density with the IMAGER, each epoch spans a comparatively long acquisition window, meaning that different patches are effectively observed at different times within the same epoch. In particular, Patch 4 is located closer to the spiral center and may therefore be sampled under a distinct timing and geometry condition, which could explain its intermittent deviations from the common trend. Moreover, the sequence consists of repeated start and stop acquisitions without prolonged settling or an uninterrupted continuous run. Therefore, the observed short-lived non-monotonic deviations may be consistent with start-up and re-initialization transients and momentary changes in effective observation conditions, finally superimposed on an overall time-dependent offset. It has to be mentioned that in these experiments, the spiral radius change of the ULi system was intentionally set to a quite slow value to maintain a comparable point density with the IMAGER.

# 5    Conclusion and outlook

This study provides a laboratory (air medium) uncertainty assessment of a special green-wavelength underwater LiDAR aka ULi system. Compared with the IMAGER used as reference sensor, the ULi system exhibits strongly non-uniform spatial sampling due to its spiral scan pattern, which must be considered when selecting evaluation patches and interpreting geometry-based metrics. Across ten repeated static scans at 2 to 5 m, plane-fit residuals remain at the millimeter level, indicating stable precision under controlled conditions. Across the usable interior of the board, the patch-wise precision is spatially homogeneous, with only slightly higher values near the outer areas, consistent with residual edge effects and local sampling or geometry differences. From 2 to 4 m the $\hat{\mu}_{\hat{\sigma}_j}$ level decreases ($\approx 1.2$ mm at 2 m and $\approx 0.9$ mm at 3 m and 4 m), while at 5 m it remains similar for most patches but shows a few localized increases. The decrease of $\hat{\mu}_{\hat{\sigma}_j}$ with increasing distance does not indicate improved intrinsic ranging noise, largely reflects the changing point-density distribution and reduced effective board coverage at longer distances, which bias the statistics toward a smaller, centrally observed subset with more consistent point density and distribution and reduce the influences of incidence angle and sampling geometry. Repeated scans confirm high repeatability of the $\hat{\mu}_{\hat{\sigma}_j}$ estimate, although the variability increases with distance and is most challenging at 5 m.

Bias analysis based on IMAGER-referenced M3C2 distances reveals consistently negative patch-wise offsets, with typical medians in the order of sub-millimeters to about ~1 mm and occasional values reaching ~1 to 2 mm. Beyond this cross-sensor offset, the epoch-wise medians exhibit a largely coherent time-dependent evolution across all patches, punctuated by short-lived non-monotonic peaks and occasional patch-specific deviations from the overall trend. The strong inter-patch coherence indicates a dominant global, time-dependent component affecting the relative ULi to IMAGER geometry during the acquisition sequence. This behavior is probably amplified by repeated start and stop the ULi between epochs and by the slow spiral scan, which couples elapsed time with observation geometry, particularly for patches located close to the spiral center. Consequently, the offsets may be best interpreted as the ULi system's internal drift. Further experiments with continuous acquisitions and increased radius-change speed are required to reduce time-geometry coupling and to confirm the magnitude and cause of the offsets.

Future work will focus on: (i) impact of sampling density on ULi precision estimates; (ii) reduce registration error between the reference TLS and the ULi system; (iii) conduct uninterrupted continuous scans without epoch restarts and increase the radius-change speed to reduce the coupling between elapsed time and observation geometry, which may help disentangle time-dependent acquisition effects from alignment-related effects and better constrain the magnitude and origin of the observed time-dependent offsets; (iv) assess the ULi's resolution capability at 2, 3, 4 and 5 m using the Boehler star (Boehler et al. 2003). Following Schmitz et al. (2020), for each web-gap segment, the foreground and background planes are fitted, classify points into foreground/background/transition based on residual thresholds. Then projecting the points into the foreground plane, and quantifying the resolution capability as the minimum distance between the foreground and background convex hulls.

# Literature

Boehler, W., Bordas Vicent, M. & Marbs, A. (2003). Investigating Laser Scanner Accuracy. Proceedings of the XIXth CIPA Symposium, Antalya, Turkey. chrome-extension://efaidnbmnnnibpcajpcglclefindmkaj/https://www.cipaheritagedocumentation.org/wp-content/uploads/2018/11/Boehler-e.a.-Investigating-laser-scanner-accuracy.pdf (Last accessed 8 Jan. 2026).

Dewez, T. J., Girardeau-Montaut, D., Allanic, C. & Rohmer, J. (2016). Facets: A cloudcompare plugin to extract geological planes from unstructured 3d point clouds. ISPRS International Archives of the Photogrammetry, Remote Sensing and Spatial Information Sciences, 41, 799-804.

Fraunhofer IPM (2025). Inspecting underwater infrastructure. Underwater Infrastructure. 3D acquisition and monitoring of large underwater structures using LiDAR. Fraunhofer Institute for Physical Measurement Techniques IPM, Freiburg, Germany. *https://www.ipm.fraunhofer.de/en/bu/object-shape-detection/ applications/underwater-laserscanning/underwater-laserscanning.html* (Last accessed 7 Jan. 2026).

Heffner, E., Walter, A. L., Scheider, A. & Sternberg, H. (2025). Laboratory-based assessment of the Underwater Laser Scanner ULi. The International Archives of the Photogrammetry, Remote Sensing and Spatial Information Sciences, 48, 123-129.

Janßen, J., Medic, T., Kuhlmann, H. & Holst, C. (2019). Decreasing the uncertainty of the target center estimation at terrestrial laser scanning by choosing the best algorithm and by improving the target design. Remote Sensing, 11(7), 845.

Lague, D., Brodu, N. & Leroux, J. (2013). Accurate 3D comparison of complex topography with terrestrial laser scanner: Application to the Rangitikei canyon (NZ). ISPRS journal of photogrammetry and remote sensing, 82, 10-26.

Neitzel, F. (2010). Generalization of total least-squares on example of unweighted and weighted 2D similarity transformation. Journal of Geodesy, 84(12), 751-762.

Petras, V., Petrasova, A., McCarter, J. B., Mitasova, H. & Meentemeyer, R. K. (2023). Point density variations in airborne LiDAR point clouds. Sensors, 23(3), 1593.

Paffenholz, J.-A. & Bae, K. H. (2012). Geo-referencing point clouds with transformational and positional uncertainties. Journal of Applied Geodesy, 6(1).

Schaffrin, B., Lee, I., Choi, Y. & Felus, Y. (2006). Total least-squares (TLS) for geodetic straight-line and plane adjustment. Bollettino di geodesia e scienze affini, 65(3), 141-168.

Schmitz, B., Kuhlmann, H. & Holst, C. (2020). Investigating the resolution capability of terrestrial laser scanners and its impact on the effective number of measurements. ISPRS Journal of Photogrammetry and Remote Sensing, 159, 41-52.

Werner, C. S., Gangelhoff, J., Frey, S., Steiger, D. & Reiterer, A. (2023). Development of a compact pulsed time-of-flight LiDAR platform for underwater measurements. The International Hydrographic Review, 29(2).

Walter, A. L., Heffner, E., Scheider, A. & Sternberg, H. (2025). Underwater laser scanning: Evaluating the performance of ULi in laboratory environments and presenting first insights from real-world applications. The International Hydrographic Review, 31(1).

Zoller+Fröhlich. (2026). Z+F IMAGER® 5016A, 3D laser scanner. *https://www.zofre.de/en/laser-scanners/3d-laser-scanner/z-f-imagerr-5016-1* (Last accessed 15 Jan. 2026).